Taylor & Francis
Taylor & Francis Group

Materials Research Letters

ISSN: 2166-3831 (Online) Journal homepage: www.tandfonline.com/journals/tmrl20

Ordered-serrated phase boundaries stabilize eutectic high-entropy alloys at high temperature

Yusha Luo , Bo Sun , Yang Tong , Ruixin Sheng , Qianqian Wang , Qihan Zheng , Zhijun Guo , Zhe Jia & Baolong Shen

To cite this article: Yusha Luo , Bo Sun , Yang Tong , Ruixin Sheng , Qianqian Wang , Qihan Zheng , Zhijun Guo , Zhe Jia & Baolong Shen (26 May 2026): Ordered-serrated phase boundaries stabilize eutectic high-entropy alloys at high temperature, Materials Research Letters, DOI: 10.1080/21663831.2026.2677722

To link to this article: https://doi.org/10.1080/21663831.2026.2677722

© 2026 The Author(s). Published by Informa UK Limited, trading as Taylor & Francis Group.

View supplementary material

Published online: 26 May 2026.

Submit your article to this journal

Article views: 7

View related articles

View Crossmark data

Full Terms & Conditions of access and use can be found at
https://www.tandfonline.com/action/journalInformation?journalCode=tmrl20

MATER. RES. LETT.
https://doi.org/10.1080/21663831.2026.2677722

ORIGINAL REPORT

OPEN ACCESS

Ordered-serrated phase boundaries stabilize eutectic high-entropy alloys at high temperature

Yusha Luo[a,b], Bo Sun[a,b], Yang Tong[c], Ruixin Sheng[a,b], Qianqian Wang[a,b], Qihan Zheng[a,b], Zhijun Guo[a,b], Zhe Jia[a,b] and Baolong Shen[a,b]

[a]School of Materials Science and Engineering, Jiangsu Key Laboratory for Advanced Metallic Materials, Southeast University, Nanjing, People's Republic of China; [b]Ministry of Education Key Laboratory of Structure and Thermal Protection for High-Speed Aircraft, Southeast University, Nanjing, People's Republic of China; [c]Advanced Studies in Precision Materials, Yantai University, Yantai, People's Republic of China

ABSTRACT
Eutectic high-entropy alloys (EHEAs) often suffer from microstructural coarsening and thermal instability at high temperatures due to weak interphase bonding. Here, we report a $CoCrFeNiTa_{0.3}$ hypoeutectic alloy with ordered-serrated phase boundaries (OSPBs) that overcomes these limitations, exhibiting 30% plasticity at ambient temperature, high yield strength of 886 MPa at 1123 K and excellent thermal stability up to $0.65T_m$. The enhanced high-temperature performance originates from the short-range ordered, low-energy, and coherent OSPBs, which stabilize eutectic boundaries, suppress softening, and coordinate interphase deformation. This study demonstrates that tailoring phase-boundary configurations is an effective strategy for developing high-temperature EHEAs with balanced strength and stability.

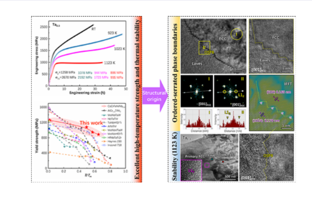

ARTICLE HISTORY
Received 18 March 2026

KEYWORDS
Labyrinthine eutectic microstructure; ordered-serrated phase boundaries; mechanical property; high temperature; thermal stability

1. Introduction

The rapid advancement of the aerospace industry imposes increasingly stringent demands on metallic materials for critical components such as turbine blades and discs, requiring robust heat resistance above 800°C [1]. Ni-based superalloys have long been the optimal candidates for these applications [2–4]. Their favorable properties arise primarily from precipitation strengthening, where coherent Ni_3X (γ' or γ'') intermetallic compounds dispersed in the γ-matrix impede dislocation motion via their high anti-phase boundary energy [5,6]. However, these Ni_3X precipitates will coarsen and transform when exposed to temperatures above 650°C, leading to alloy degradation. Consequently, further performance improvements in such materials are approaching their inherent limits. Eutectic high-entropy alloys containing refractory elements such as Nb, Ta, and Zr can form thermally stable Laves phases in the as-cast state, emerging as promising candidates for high-temperature environments [7–9]. At fully eutectic composition, the well-established $CoCrFeNiNb_{0.45}$ and $CoCrFeNiTa_{0.4}$ alloys exhibit superior compressive yield strengths of 1618 and 1091 MPa at 973 K, respectively, but undergo severe softening beyond this temperature [10]. The dense eutectic phase boundaries can become preferential sites for diffusion-assisted creep and interfacial sliding,

CONTACT Baolong Shen blshen@seu.edu.cn School of Materials Science and Engineering, Jiangsu Key Laboratory for Advanced Metallic Materials, Southeast University, Nanjing 211189, People's Republic of China; Ministry of Education Key Laboratory of Structure and Thermal Protection for High-Speed Aircraft, Southeast University, Nanjing 211189, People's Republic of China; Qianqian Wang qwang678@seu.edu.cn School of Materials Science and Engineering, Jiangsu Key Laboratory for Advanced Metallic Materials, Southeast University, Nanjing 211189, People's Republic of China; Ministry of Education Key Laboratory of Structure and Thermal Protection for High-Speed Aircraft, Southeast University, Nanjing 211189, People's Republic of China; Zhijun Guo zj-guo@seu.edu.cn School of Materials Science and Engineering, Jiangsu Key Laboratory for Advanced Metallic Materials, Southeast University, Nanjing 211189, People's Republic of China; Ministry of Education Key Laboratory of Structure and Thermal Protection for High-Speed Aircraft, Southeast University, Nanjing 211189, People's Republic of China

Supplemental data for this article can be accessed online at https://doi.org/10.1080/21663831.2026.2677722.

© 2026 The Author(s). Published by Informa UK Limited, trading as Taylor & Francis Group.
This is an Open Access article distributed under the terms of the Creative Commons Attribution License (http://creativecommons.org/licenses/by/4.0/), which permits unrestricted use, distribution, and reproduction in any medium, provided the original work is properly cited. The terms on which this article has been published allow the posting of the Accepted Manuscript in a repository by the author(s) or with their consent.

thereby contributing to macroscopic softening. While they provide strong room-temperature strengthening, weak semi-coherent bonding [11] promotes microstructural instability and coarsening at elevated temperatures. Thus, rationally regulating these phase boundaries, either by optimizing density or tailoring interfacial structure, is essential for high-temperature application of EHEAs.

To overcome weak interfacial bonding in high-temperature structural materials, a promising strategy is to design low-energy serrated interfaces, which are known to improve creep resistance and suppress crack propagation [12]. Such interfaces can be constructed through various processing routes, including investment casting followed by post-casting heat treatments [13], powder metallurgy, and thermomechanical forging coupled with controlled cooling treatments [14]. The driving force for serration is primarily attributed to the reduction in interfacial free energy, as these boundaries consist of segments preferentially aligned along low-index {111} planes [14–16]. While the detailed formation and growth mechanisms of serrated interfaces remain under investigation, prevailing explanations point to interactions between grain boundaries (GBs) and second-phase particles [17,18], such as γ' precipitates in Ni-based superalloys [13] or $M_{23}C_6$ carbides in stainless steels [19]. Alternatively, serration has also been attributed to the accumulation of lattice strain energy near GBs resulting from elemental diffusion and segregation, a mechanism that can operate even in the absence of second phases [20]. Efforts to design eutectic serrated phase boundaries in the $Re_{0.5}MoNbW(TaC)_{0.5}$ alloy have proven viable, raising its yield strength from 500 to 900 MPa at 1473 K [21]. Nonetheless, this strengthening is accompanied by a high fraction and large size of ceramic phases, resulting in room-temperature embrittlement and elevated density. Therefore, to fully harness the benefits of serrated interfaces without introducing detrimental brittleness, it is imperative to explore alternative microstructural designs that minimize or eliminate coarse ceramic reinforcements.

In this paper, we present a novel hypoeutectic $CoCrFeNiTa_{0.3}$ alloy featuring in-situ formed ordered-serrated phase boundaries (OSPBs) between ductile and hard metallic phases. This alloy exhibits an excellent strength–plasticity synergy from ambient temperature to 1123 K, along with remarkable thermal stability up to $\sim 0.65T_m$. The integration of a labyrinthine eutectic structure with Ta segregation-induced interfacial $L1_2$ short-range orders promotes the formation of OSPBs. The coherent OSPBs act as a strain mediator between the soft FCC and hard Laves phases, enhancing strain accommodation capability. Furthermore, the ordered $L1_2$ clusters at OSPBs strengthen the interfacial cohesion, thereby overcoming the strength-plasticity trade-off across a wide temperature range, which is inherent in previously developed EHEAs.

2. Materials and methods

A set of $CoCrFeNiTa_x$ EHEAs with 0.3 at.% Ta, 0.4 at.% Ta and 0.5 at.% Ta (denoted as $Ta_{0.3}$, $Ta_{0.4}$, and $Ta_{0.5}$) were manufactured by using arc-melting in a Ti-gettered argon atmosphere. Each ingot was turned over and remelted five times to reduce compositional inhomogeneity, then suction into a cylindrical alloy column with a diameter of 3 mm. Compression tests were performed on cylindrical specimens with dimensions of Φ 3 × 5 mm at a constant strain rate of 10^{-3} s^{-1}. Room-temperature (298 K) compression tests were conducted using an Instron 5982 testing system, while the elevated temperature tests were carried out under pure argon in a vacuum furnace using a Sans UTM5305H machine. To ensure statistical reliability, three samples were tested for each condition.

The crystal structure was identified by the X-ray diffraction (XRD, Bruker D8-Discover) with Cu $K\alpha$ radiation, scanning in the 2θ range of 20° to 100° at a rate of 4°/min. The microstructural and interfacial characterizations of the alloys were performed by transmission electron microscopy operating at 200 kV (TEM, Thermofisher F200X) equipped with selected area electron (SAED) and energy dispersive spectroscopy (EDS) detectors. High-angle annular dark field (HAADF)-STEM imaging was performed with a collection angle between 30° and 60° mrad. The TEM samples were prepared by ion milling (GATAN-M691). The volume fractions of the FCC and Laves phases were determined by analyzing a minimum of 15 TEM images per alloy composition ($Ta_{0.3}$, $Ta_{0.4}$, and $Ta_{0.5}$) using Image J software.

3. Results and discussion

3.1. Mechanical properties over a wide temperature range

Uniaxial compressive tests at both room temperature (RT) and 1123 K were performed on as-cast $CoCrFeNiTa_x$ EHEAs (x = 0.3, 0.4, and 0.5 at.%, corresponding to hypoeutectic, eutectic, and hypereutectic microstructures, respectively). The resulting engineering stress versus strain curves are presented in Figure 1(a and b). At RT, the $Ta_{0.4}$ alloy exhibits a yield strength (σ_y) of 1932MPa, and $Ta_{0.5}$ alloy reaches 2161 MPa. Despite a slightly lower yield strength (1258 MPa), the $Ta_{0.3}$ alloy achieves superior fracture strength (σ_{CS}) due to its exceptional work hardening capacity and a three-fold higher plasticity (ε_p) over other alloys. At 1123 K, the $Ta_{0.4}$ and $Ta_{0.5}$ alloys demonstrate yield strengths of

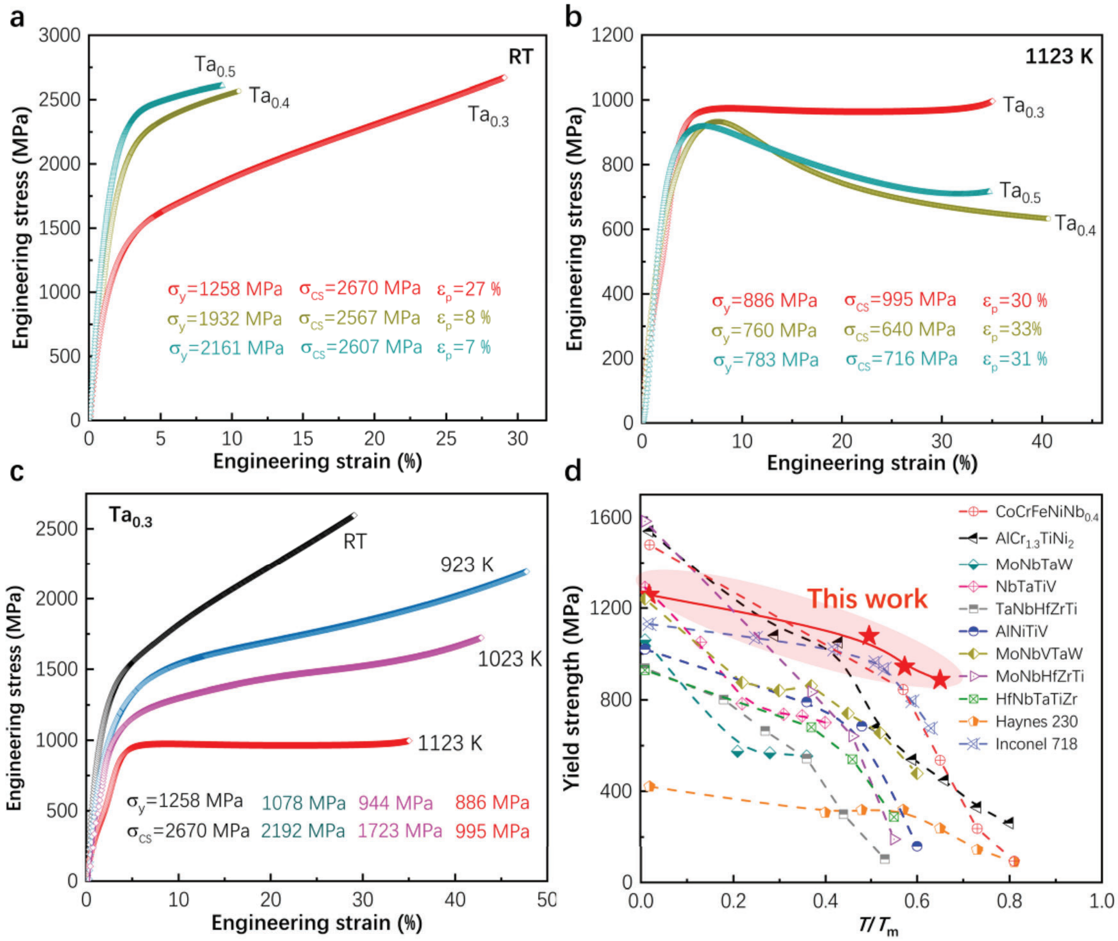

Figure 1. Mechanical properties of Ta_x EHEAs. Stress–strain curves of the $Ta_{0.3}$ (hypoeutectic), $Ta_{0.4}$ (eutectic) and $Ta_{0.5}$ (hypereutectic) alloys at (a) room temperature (RT) and (b) 1123 K. Plots for the $Ta_{0.3}$ alloy showing (c) temperature-dependent properties (RT–1123 K) and (d) yield strength (σ_y) evolution with homologous temperature (T/T_m). All other reference data are from compression tests, while Haynes 230 and Inconel 718 are from tension tests.

760 and 783 MPa, respectively, while their compressive strengths are 640 and 716 MPa, showing an obvious softening behavior. In contrast, the $Ta_{0.3}$ alloy exhibits the distinct strengthening behavior, registering an outstanding high yield strength of 886 MPa, an ultimate compressive strength of 995 MPa, and a plasticity exceeding 30% without fracture. Notably, the $Ta_{0.3}$ alloy exhibits a good combination of high strength and remarkable softening resistance at 1123 K.

To evaluate the temperature dependence of the mechanical properties of the $Ta_{0.3}$ alloy, compressive tests were performed at 298, 923, 1023 and 1123 K (Figure 1(c)). The results demonstrate that the $Ta_{0.3}$ alloy possesses excellent plasticity, with compressive strains exceeding 30% at all tested temperatures. It exhibits superior resistance to intermediate-temperature embrittlement [22,23], a common issue that causes severe brittleness in many high-temperature alloys within the 873–1073 K. Although the yield strengths gradually decrease with increasing temperature, they maintain rather high levels at elevated temperatures, with values of 1078 MPa at 923 K, 944 MPa at 1023 K, and 886 MPa at 1123 K. In Figure 1(d), we summarize the temperature dependence of yield strength, expressed as homologous temperature, i.e. the ratio of testing temperature/melting temperature (T/T_m), and compare it with representative EHEAs [24], RHEAs [25–29], and conventional superalloys [30]. Generally, the softening will occur in an alloy when the temperature is above 0.5–0.6T_m due to the activation of diffusion-controlled deformation mechanisms [31]. For instance, although $AlCr_{1.3}TiNi_2$ alloy has an outstanding yield strength from 298 K to 873 K [32] (T/T_m ∼ 0.45) among the investigated alloys, it softens rapidly with the further increase of temperature. However, the present $Ta_{0.3}$ alloy deviates from this trend, as it exhibits higher strength above 0.6 T/T_m. These results clearly confirm that $Ta_{0.3}$ alloy holds a prominent position among advanced structural materials reported in the literature.

3.2. Ordered-serrated phase boundaries

The microstructure, chemical composition, and phase boundary features of the $Ta_{0.3}$, $Ta_{0.4}$, and $Ta_{0.5}$ alloys were systematically unraveled by XRD and TEM (Figures 2, 3, and S1–S3). The XRD patterns (Figure 2(a) and S1) exhibit that all the alloys are composed of FCC and Laves dual-phase structures. As the Ta content increases, the weakening of the FCC peaks and the concurrent strengthening of the Laves phase indicate a shift in their relative volume fractions. This trend is further corroborated by the distinct microstructural morphologies observed in the corresponding bright-field (BF) TEM images across the three alloys. Specifically, the $Ta_{0.3}$ hypoeutectic alloy forms eutectic colonies alongside a bright primary phase (Figure 2(b)). These eutectic colonies constitute a labyrinthine morphology that is developed only within a narrow compositional window [33]. Selected area electron diffraction (SAED) patterns confirm that these bright and dark regions, obtained along the [110] and $[2\bar{1}\bar{1}0]$ zone axes, correspond to FCC and Laves structures, respectively. The STEM-EDS results in Figure 3(c) reveal the compositional information of both eutectic phases and primary phases. Notably, Ni, Cr, and Fe preferentially partition into the FCC phase, while Co and Ta are predominantly enriched in the Laves phase. One-dimensional concentration profiles along the white arrows in Figure 2(c) demonstrate that primary FCC phases exhibit higher Ta content compared to their eutectic counterparts. Their compositions are summarized in Supplementary Table S1. In hypoeutectic alloys, the primary FCC phase gains Ta from the liquid via local solute redistribution, whereas during eutectic solidification Ta partitions preferentially into the Laves phase [34], leading to a lower Ta level in the eutectic FCC phase than in the primary FCC phase. It is inverse in hypereutectic alloys; the primary Laves phase forms first [35], enriching most Ta and leaving the remaining liquid Ta-depleted, resulting in a lower Ta content in the eutectic Laves phase (Fig. S3).

A distinctive ordered-serrated phase boundaries (OSPBs) is discovered in the $Ta_{0.3}$ alloy (Figure 2(d)). Its short-range ordering feature, confirmed by the FFT patterns and corresponding intensity profile at the under layer, reveals the formation of an $L1_2$-ordered structure (Figure 2(d) and Fig. S4). A magnified high-resolution (HR) TEM image taken along the $[001]_{FCC}$ zone axis clearly exhibits the serrated morphology (Figure 2(e)). Serrated grain boundaries (SGBs) are known to suppress grain boundary sliding, promote intragranular deformation, delay crack propagation across a wide temperature range [12, 36], enhance creep resistance [37], and mitigate intermediate-temperature intergranular embrittlement [23]. The inverse fast Fourier transform (IFFT) image (Figure 2(f)) and Fig. S5 show a near-perfectly coherent state between the $(020)_{FCC}$ and $(10\bar{1}4)_{Laves}$ planes at the OSPB, where periodic dislocations accommodate the slight lattice mismatch, forming a low-energy coherent interface [11]. In Figure 2(g–h), short-range ordered $L1_2$ phases are present at nearly all OSPBs, indicating a mutual promotion between the serrated interface and secondary phases [18]. The ordered $L1_2$ structures enhance interfacial cohesion and contribute to improved high-temperature stability and intergranular degradation resistance. Overall, the OSPB serves a key role that enhances both room-temperature plasticity and high-temperature strength by promoting interface strengthening and strain accommodation.

In contrast, a fully eutectic microstructure is observed in the $Ta_{0.4}$ alloy (Figure 3(a)), characterized by regularly alternating FCC and Laves lamellae with uniform thickness. Systematic observations of the eutectic interfaces reveal the straight, semi-coherent phase boundaries (Figure 3(b)). There are no short-range ordered structures within these regions, instead there are nanoscale atomic misalignment zones (Figure 3(c)). This type of interfacial configuration features moderate lattice mismatch and possesses semicoherent strain energy, contributing to material strengthening through dislocation pinning, while simultaneously acting as a potential site for crack initiation due to its limited interfacial bonding strength [11, 34]. When the Ta content reaches 0.5, a hypereutectic microstructure forms, featuring primary Laves phase alongside irregular eutectic colonies (Figure 3(d)). It is noted that the primary phases appear only in the hypo- and hypereutectic alloys. And the grain sizes of the primary FCC or Laves phases (Figures 2(b) and 3(d)) are larger than their counterparts in the eutectic colonies. Furthermore, the volume fractions of the FCC and Laves phases are 81% and 19% in the $Ta_{0.3}$ alloy, 62% and 38% in the $Ta_{0.4}$ alloy, and 30% and 70% in the $Ta_{0.5}$ alloy, respectively. In hypereutectic alloys, phase boundaries similarly exhibit a straight morphology (Figure 3(e)), yet they are incoherent without short-range ordered structures or atomic rearrangement zones (Figure 3(f)). It is worth noting that the interface between the finer eutectic Laves phase and the FCC phase remains predominantly semi-coherent. In other words, the phase boundaries in $Ta_{0.5}$ alloy are a mixture of semi-coherent and incoherent types. These high-energy interfaces strongly impede dislocation motion during deformation, but simultaneously promote stress concentration

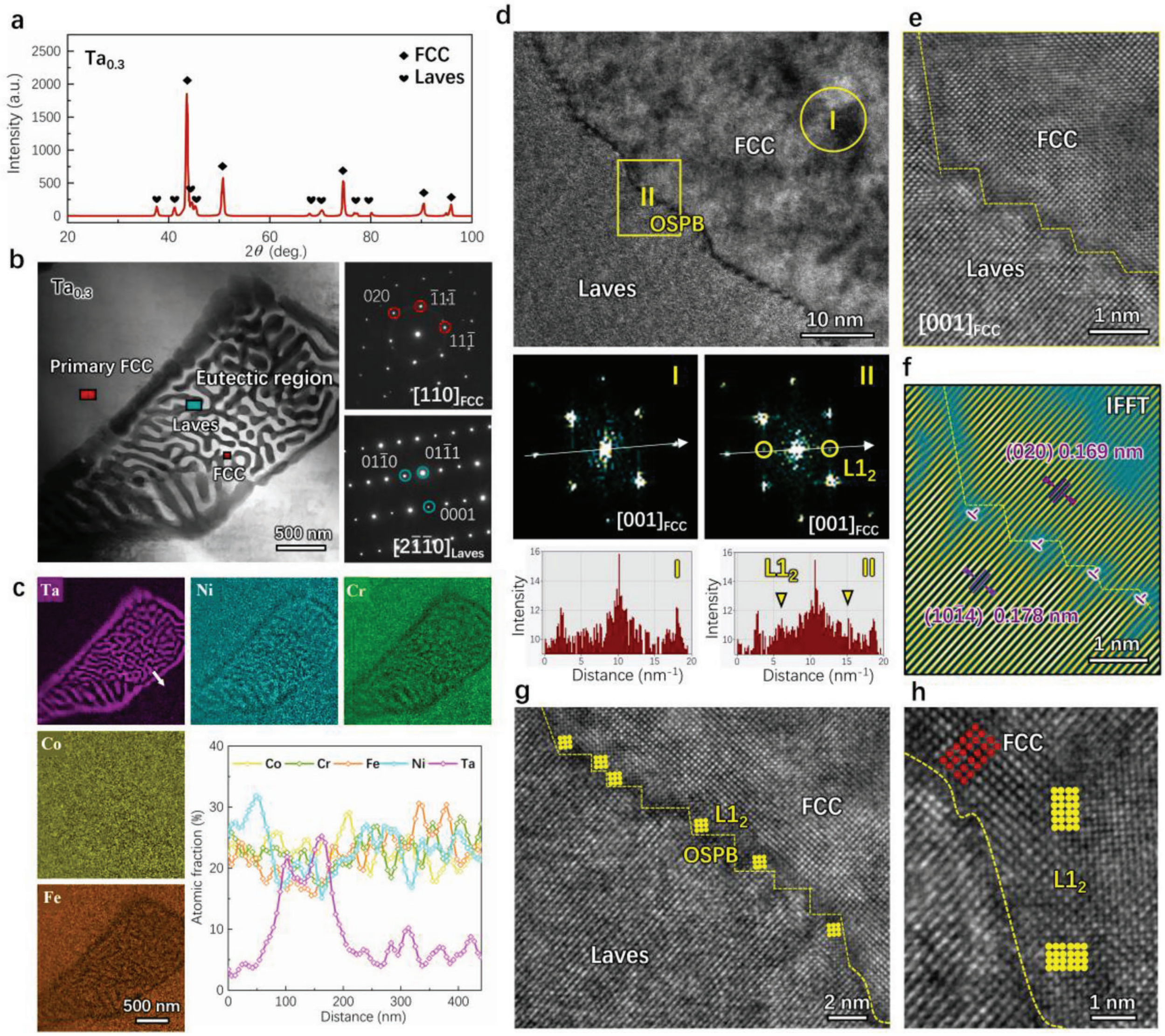

Figure 2. Microstructure and OSPB in $Ta_{0.3}$ alloy. (a) Phase identification via XRD pattern. (b) The hypoeutectic structure and its dual-phase diffraction patterns and (c) the corresponding EDS mappings, line-scanning element analysis recorded along the white line for Co, Cr, Fe, Ni, and Ta. (d) HAADF image of OSPB morphology and the corresponding FFT patterns of I and II, along with the intensity profile measured along the white arrow, are displayed in the bottom row. (e) Enlarged image of OSPB. (f) Coherent characteristic and periodic dislocations of the OSPB, (g-h) ordered feature of the OSPB.

and phase boundary migration, thereby elevating fracture susceptibility and compromising high-temperature stability [38].

The absence of OSPBs in the $Ta_{0.4}$/$Ta_{0.5}$ alloys, in contrast to the $Ta_{0.3}$ alloy, is attributed to distinct solidification paths and Ta partitioning behaviors [7]. In the $Ta_{0.3}$ alloy, the primary FCC phase that is poor in Ta (Figure 2(c)) solidifies first across a relatively wide temperature range. Since Ta (with partition coefficient $k < 1$) is rejected into the liquid, it progressively enriches the remaining liquid, forming a solute-rich boundary layer. This enrichment induces constitutional undercooling, which in turn facilitates the formation of serrated phase boundaries [39]. Furthermore, the ensuing eutectic reaction under such Ta-rich conditions promotes $L1_2$ short-range ordering at the FCC/Laves interfaces. Then, the $L1_2$ nanodomains act as pinning sites, impeding boundary migration during solidification and inducing the serrated morphology [40]. In the $Ta_{0.4}$ alloy, solidification proceeds isothermally via the eutectic reaction. Under such near-equilibrium conditions, the coupled growth of the two phases dominates the interface morphology. This cooperative growth mechanism favors the formation of a regular lamellar structure with flat interfaces to maintain efficient diffusion coupling and minimize the total interfacial energy [41]. In the $Ta_{0.5}$ alloy, the primary Laves phase is intrinsically Ta-rich (Fig. S3).

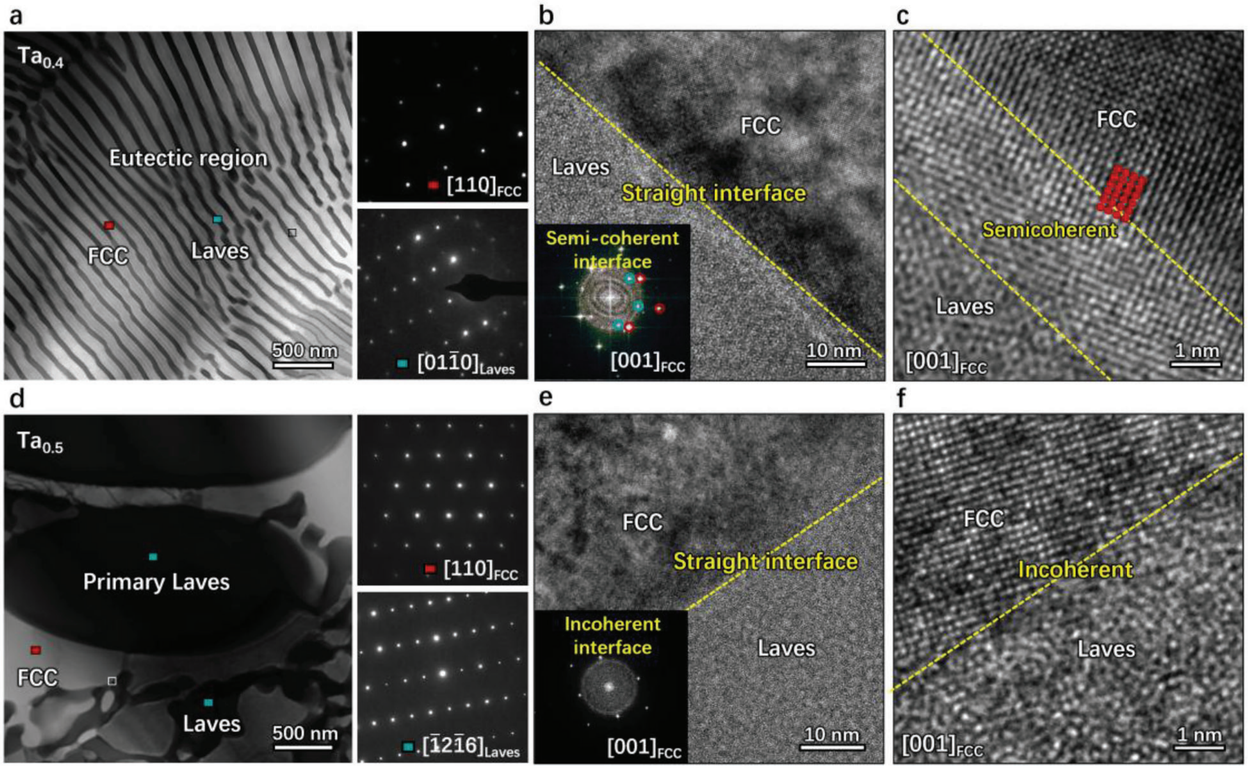

Figure 3. Phase boundary characteristics in $Ta_{0.4}$ and $Ta_{0.5}$ alloys. (a–c) $Ta_{0.4}$ alloy: (a) Lamellar eutectic colony morphology and corresponding SAED patterns of the FCC and Laves phases. (b) A typical straight phase boundary (SPB) exhibiting a semi-coherent relationship. (c) HRTEM image of the SPB, showing the absence of short-range ordered structures. (d-f) $Ta_{0.5}$ alloy: (d) Hypereutectic microstructure and corresponding SAED patterns. (e) Prevalent straight phase boundary with an incoherent relationship. (f) HRTEM image confirming the lack of short-range ordering at the incoherent boundary.

Consequently, Ta preferentially partitions into the primary Laves phase during solidification. This preferential partitioning consumes most of the Ta early in solidification, leaving the remaining liquid Ta-depleted and thus suppressing constitutional undercooling at the subsequent eutectic growth front, which hinders the formation of serrated phase boundaries. In addition, the Ta-depleted conditions suppress $L1_2$ short-range ordering at the FCC/Laves interfaces, which in turn inhibits OSPBs formation. The primary Laves phase also acts as a physical constraint, limiting the subsequent eutectic growth within its interstices.

3.3. Phase and OSPB stabilities at 1123 K

To elucidate the origin of the superior high-temperature performance of the $Ta_{0.3}$ alloy, the microstructures of the three alloys deformed at 1123 K were characterized. The $Ta_{0.3}$ alloy exhibits an $L1_2$-strengthened primary FCC phase, and the eutectic region maintains its morphology despite slight coarsening, indicating excellent microstructural stability at 1123 K (Figure 4(a)). In the $Ta_{0.4}$ alloy (Figure 4(b)), the original eutectic lamellae undergo coarsening, fragmentation, and recrystallization. While the primary Laves phase in the $Ta_{0.5}$ alloy remains relatively stable, the initially disordered eutectic region also exhibits evident recrystallization and phase transformation (Figure 4(c)). For a more direct comparison of microstructural stability among the three alloys, the recrystallized fraction and the coarsening degree of the eutectic regions were quantified in Figure 4(d). The fully eutectic microstructure exhibits the lowest stability, characterized by the highest recrystallized fraction and severe lamellar coarsening. In contrast, the hypereutectic structure shows less eutectic coarsening but a higher recrystallized fraction than the hypoeutectic alloy. The recrystallized volume fraction is closely correlated with the melting points of the constituent phases, which were calculated using the rule of mixtures based on their actual compositions, as presented in Figure 4(e). It can be observed that the melting points of both the primary FCC phase and the eutectic Laves phase in the $Ta_{0.3}$ alloy are higher than those of the corresponding phases in the other alloys, which partially accounts for its superior microstructural stability at elevated temperatures.

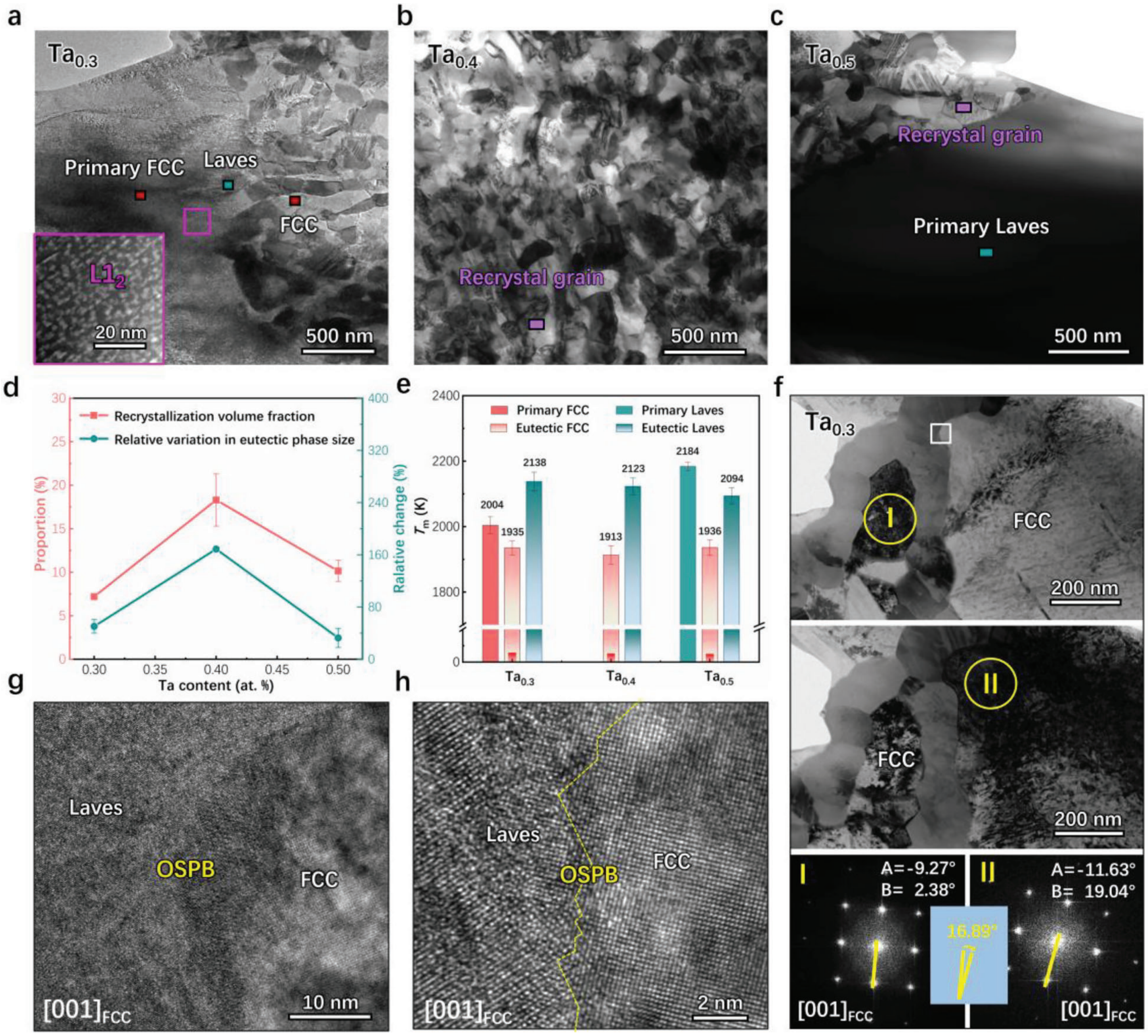

Figure 4. Phase and OSPB stability at 1123 K. BF images of (a) $Ta_{0.3}$, (b) $Ta_{0.4}$, and (c) $Ta_{0.5}$ alloys, respectively, reflecting the phase stability. (d) Quantitative variation of recrystallization volume fraction and relative eutectic phase size with Ta content. (e) Melting points of primary FCC, primary Laves, eutectic FCC, and eutectic Laves phases across the three alloys. (f) The angular misorientation between the two sides of the serrated phase boundary was quantified by tilting each region to its respective zone axis. For region I, the α and β tilt angles were −9.27° and 2.38°, respectively. Region II was aligned with tilt angles of −11.63° and 19.04°. (g-h) A stable OSPB observed after deformation at 1123 K.

In addition, the OSPB provides a further contribution to the high-temperature phase stability. Figure 4(f) displays the misorientation between the grains on both sides of the OSPB (Region I and Region II) after deformation at 1123 K. When the zone axis of region I is aligned, the corresponding α and β angles are –9.27° and 2.38°, respectively, while for region II they are –11.63° and 19.04°. The considerable angular difference confirms that high-angle grain boundary (HAGB) exists across the OSPB. The significant misorientation suggests that the OSPB preferentially forms at high-angle grain boundaries, which aligns with the findings of Jeong [17]. This behavior stems from the high interfacial energy characteristic of high-angle grain boundaries, which promotes interface serration as a mechanism to lower the overall energy. After compression at 1123 K, the OSPB remained observable in the microstructure (Figure 4(g and h)), demonstrating its intrinsic high-temperature stability. This stable interface also effectively pins the high-temperature phases, suppressing their coarsening and transformation [42]. Importantly, long-term annealing of the $Ta_{0.3}$ alloy at 1123 K for durations of 1 and 6 h resulted in only minor changes to the phase morphology, OSPBs, and mechanical properties (Fig. S6), confirming its excellent thermal stability.

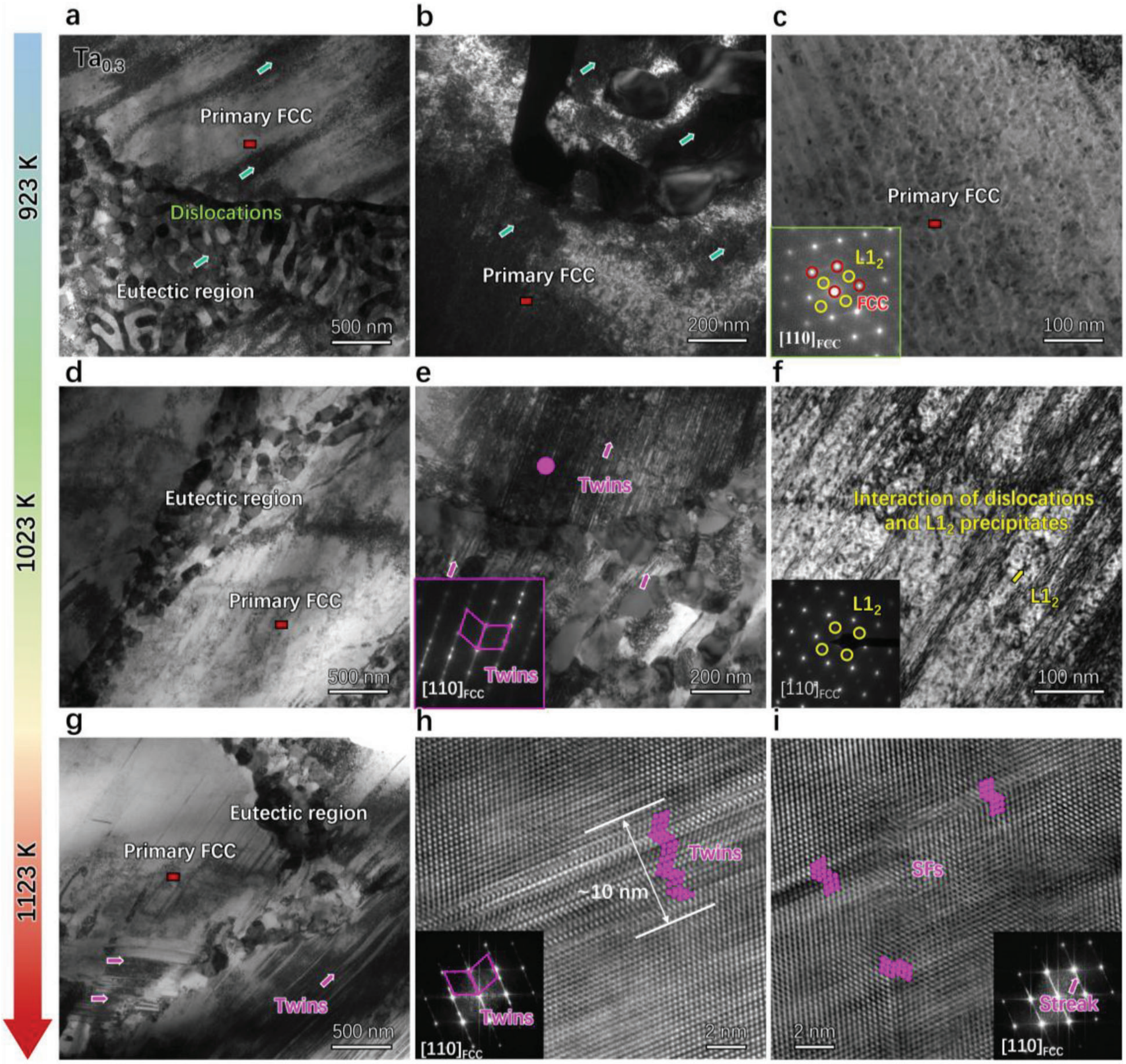

Figure 5. High-temperature deformation mechanism of $\text{Ta}_{0.3}$ alloy. (a–c) Deformation microstructure at 923 K. (a) Primary FCC and eutectic phases retain morphology, (b) dense dislocations in FCC phase, eutectic deforms locally without twinning, (c) L1_2 precipitates cut dislocations. (d–f) Deformation microstructure at 1023 K. (d) Stable morphology is maintained, (e) twins and dislocations coexist in FCC, and interfacial defects are present in the eutectic, (f) twin-L1_2 interaction subdivides the dislocation structure. (g–i) Deformation microstructure at 1123 K. (g) The activation of more twins and their interaction with dislocations, (h–i) the twin size increases in FCC, and SFs assist deformation.

It is worth noting that the $\text{Ta}_{0.3}$, $\text{Ta}_{0.4}$, and $\text{Ta}_{0.5}$ alloys exhibit substantial differences in FCC/Laves phase fractions, primary FCC or Laves, and eutectic morphology (labyrinthine, regular lamellar/irregular). These microstructural features undoubtedly affect mechanical properties at RT or 1123 K. However, the nature of phase boundaries is the most fundamental and critical factor tailoring the mechanical behavior. That is, without OSPBs, the alloy would readily crack along phase boundaries at RT or undergo microstructural coarsening at elevated temperatures, resulting in structural degradation and unstable mechanical performance.

3.4. *High-temperature deformation mechanism of hypoeutectic alloy*

To elucidate the mechanisms behind its high compressive plasticity and intermediate-temperature embrittlement resistance, the high-temperature deformation substructure of the $\text{Ta}_{0.3}$ alloy was observed in Figure 5. After compression at 923 K, both the primary FCC phase and the eutectic region largely retained their original morphology without noticeable grain coarsening, recrystallization, or structural instability (Figure 5(a)). Extensive dislocation tangles, forming planar slip bands, were observed within the primary FCC phase (Figure 5(b)), which accounts for its excellent work hardening ability. In contrast, within the eutectic region, deformation is cooperatively accommodated by both the Laves and FCC phases. During the initial stage of deformation, the softer FCC phase yields first, undergoing plastic strain primarily through dislocation slip and multiplication, thereby bearing the majority of the applied strain and transferring stress to the surrounding Laves phase (Fig. S7) [11, 34]. As strain increases, the hard Laves phase progressively becomes the dominant load-bearing constituent. It accommodates macroscopic deformation through mechanisms such as elastic bending, coordinated rotation, and the initiation of microcracks [43,44], which helps to alleviate local stress concentrations and delay premature fracture. Due to its intrinsic brittleness, the Laves phase exhibits very limited intrinsic plastic deformability [45], with its deformation dominated by these brittle accommodation mechanisms rather than by dislocation-mediated slip. Although $L1_2$ ordered precipitates are present in the primary FCC phase (Figure 5(c)), they not only effectively impede dislocation motion but also positively contribute to the overall high-temperature performance. After compression at 1023 and 1123 K, the microstructure remains stable (Figure 5(d and g)). Deformation twins are observed at both temperatures, with the twin width increasing as the temperature rises (Figure 5(e and h)). The interaction between dislocations, stacking faults, twins, and the $L1_2$ precipitates (Figure 5(f and i)) plays a crucial role in the strengthening mechanisms and strain-hardening behavior of the $Ta_{0.3}$ alloy.

In addition, the OSPB play a critical role in coordinating deformation and facilitating stress transfer between the hard Laves phase and the ductile FCC matrix, a function that is equally operative at RT. Consequently, the phase fraction is not the decisive factor for ductility. If it were, $Ta_{0.4}$ and $Ta_{0.5}$ would show markedly different plasticity given their large difference in phase fractions, yet their plasticity is comparable (Figure 1(a)). The periodically ordered, serrated interface structure provides a larger effective interfacial area and enhances mechanical interlocking, which strengthens bonding and reduces the risk of interfacial decohesion [46,47]. During deformation, the serrated morphology promotes progressive, stable yielding by inducing multi-directional stress concentrations that promote activation of multiple slip systems in the adjacent FCC phase. This helps to distribute strain more uniformly and delays localized stress buildup. Furthermore, the ordered interfacial structure acts as an effective barrier to dislocation motion, causing dislocations to accumulate and rearrange near the boundary. This not only enhances strain hardening but also enables efficient stress transfer from the softer FCC phase to the harder Laves phase through shear and normal stress components along the interlocked boundary facets [48]. The OSPB thereby mitigates strain incompatibility, suppresses interfacial cracking, and contributes significantly to the alloy's sustained plasticity and strength under mechanical loading.

4. Conclusion

In summary, we developed a hypoeutectic alloy with ordered-serrated phase boundaries, achieving a remarkable combination of excellent plasticity, considerable high-temperature strength, and superior thermal stability. The nanoscale ordered-serrated structure at phase boundaries plays a critical role in strengthening interfaces, mediating strain delocalization, and activating multiple-deformation mechanisms. Further, the solidification sequence of the primary and eutectic phases strongly dictates the distribution of the high-melting-point Ta, thereby raising the melting points of constituent phases and improving the microstructural stability of the hypoeutectic alloy. This interface modulation strategy provides a viable route for developing structural materials suitable for high-temperature applications.

Author contributions

CRediT: **Yusha Luo:** Data curation, Formal analysis, Investigation, Methodology, Validation, Visualization, Writing – original draft; **Bo Sun:** Conceptualization, Methodology, Software; **Yang Tong:** Data curation, Investigation, Resources; **Ruixin Sheng:** Investigation, Methodology; **Qianqian Wang:** Funding acquisition, Supervision, Visualization, Writing – review & editing; **Qihan Zheng:** Conceptualization, Investigation; **Zhijun Guo:** Funding acquisition, Project administration, Resources; **Zhe Jia:** Funding acquisition, Resources, Supervision; **Baolong Shen:** Funding acquisition, Project administration, Resources, Supervision, Writing – review & editing

Disclosure statement

No potential conflict of interest was reported by the author(s).

Funding

This work was supported by the National Natural Science Foundation of China [52231005, 52571183, 52371164].

References

[1] Reed RC. The superalloys fundamentals and applications [M]. Cambridge: Cambridge University Press; 2006.

[2] Mazumder N, Kumar D, Singh MP, et al. Synergistic effect of multimodal γ' precipitates tuned through Ti addition on phase stability and strength of Co-Ni based superalloy. Scr Mater. 2023;223:115105. doi:10.1016/j.scriptamat.2022.115105

[3] Zhang J, Huang T, Lu F, et al. Unveiling the Re-segregation at the γ/γ' interface in a Ni-based superalloy. Scr Mater. 2021;204:114131. doi:10.1016/j.scriptamat.2021.114131

[4] Kovarik L, Unocic RR, Li J, et al. Microtwinning and other shearing mechanisms at intermediate temperatures in Ni-based superalloys. Prog Mater Sci. 2009;54:839–873. doi:10.1016/j.pmatsci.2009.03.010

[5] Shi R, McAllister DP, Zhou N, et al. Growth behavior of γ'/γ'' coprecipitates in Ni-base superalloys. Acta Mater. 2019;164:220–236. doi:10.1016/j.actamat.2018.10.028

[6] Guo Y, Liu B, Xie W, et al. Anti-phase boundary energy of β series precipitates in Mg-Y-Nd system. Scr Mater. 2021;193:127–131. doi:10.1016/j.scriptamat.2020.11.004

[7] Ai C, He F, Guo M, et al. Alloy design, micromechanical and macro mechanical properties of CoCrFeNiTa$_x$ eutectic high entropy alloys. J Alloys Compd. 2018;735:2653–2662. doi:10.1016/j.jallcom.2017.12.015

[8] Chanda B, Das J. Evolution of microstructure homogeneity and mechanical properties in nano-/ultrafine eutectic CoCrFeNiNb ($0.45 \leq x \leq 0.65$) high entropy alloy ingots and cast rods. J Alloys Compd. 2022;901:163610. doi:10.1016/j.jallcom.2022.163610

[9] He F, Wang Z, Shang X, et al. Stability of lamellar structures in CoCrFeNiNb$_x$ eutectic high entropy alloys at elevated temperatures. Mater Des. 2016;104:259–264. doi:10.1016/j.matdes.2016.05.044

[10] Chanda B, Pani SK, Das J. Mechanism of microstructure evolution and spheroidization in ultrafine lamellar CoCrFeNi (Nb$_{0.5}$/Ta$_{0.4}$) eutectic high entropy alloys upon hot deformation. Mater Sci Eng A. 2022;835:142669. doi:10.1016/j.msea.2022.142669

[11] Luo Y, Wang Q, Sun B, et al. Deformable eutectic alloy with near-theoretical yield strength via hierarchical nanoscale multiphases and sessile defects. Adv Sci. 2026;13:e18764. doi:10.1002/advs.202518764

[12] Son H-W, Lee J-W, Hyun S-K. Mechanism of grain boundary serration during hot deformation of AZ31 alloy: role of grain boundary dislocations and grain boundary sliding. Int J Plast. 2020;125:118–132. doi:10.1016/j.ijplas.2019.09.003

[13] Koul AK, Thamburaj R. Serrated grain boundary formation potential of Ni-based superalloys and its implications. Metall Trans A. 1985;16:17–26. doi:10.1007/BF02656707

[14] Hong HU, Jeong HW, Kim IS, et al. Significant decrease in interfacial energy of grain boundary through serrated grain boundary transition. Philos Mag. 2012;92:2809–2825. doi:10.1080/14786435.2012.676212

[15] Hong HU, Kim IS, Choi BG, et al. The effect of grain boundary serration on creep resistance in a wrought nickel-based superalloy. Mater Sci Eng A. 2009;517:125–131. doi:10.1016/j.msea.2009.03.071

[16] Lee JW, Kim DJ, Hong HU. A new approach to strengthen grain boundaries for creep improvement of a Ni–Cr–Co–Mo superalloy at 950 °C. Mater Sci Eng A. 2015;625:164–168. doi:10.1016/j.msea.2014.12.010

[17] Jeong CY, Kim KJ, Hong HU, et al. Effects of aging temperature and grain size on the formation of serrated grain boundaries in an AISI 316 stainless steel. Mater Chem Phys. 2013;139:27–33. doi:10.1016/j.matchemphys.2012.11.021

[18] Lee JW, Terner M, Hong HU, et al. A new observation of strain-induced grain boundary serration and its underlying mechanism in a Ni–20Cr binary model alloy. Mater Charact. 2018;135:146–153. doi:10.1016/j.matchar.2017.11.047

[19] Hong HU, Nam SW. The occurrence of grain boundary serration and its effect on the M$_{23}$C$_6$ carbide characteristics in an AISI 316 stainless steel. Mater Sci Eng A. 2002;332:255–261. doi:10.1016/S0921-5093(01)01754-3

[20] Yoon JG, Jeong HW, Yoo YS, et al. Influence of initial microstructure on creep deformation behaviors and fracture characteristics of Haynes 230 superalloy at 900°C. Mater Charact. 2015;101:49–57. doi:10.1016/j.matchar.2015.01.002

[21] Wei Q, Xu X, Shen Q, et al. Metal-carbide eutectics with multiprincipal elements make superrefractory alloys. Sci Adv. 2022;8:2068. doi:10.1126/sciadv.abo2068

[22] Hou JX, Liu SF, Cao BX, et al. Designing nanoparticles-strengthened high-entropy alloys with simultaneously enhanced strength-ductility synergy at both room and elevated temperatures. Acta Mater. 2022;238:118216. doi:10.1016/j.actamat.2022.118216

[23] Zhou YH, Zhang JY, Zhang J, et al. A strong-yet-ductile high-entropy alloy in a broad temperature range from cryogenic to elevated temperatures. Acta Mater. 2024;268:119770. doi:10.1016/j.actamat.2024.119770

[24] Jiang H, Qiao D, Lu Y, et al. Direct solidification of bulk ultrafine-microstructure eutectic high-entropy alloys with outstanding thermal stability. Scr Mater. 2019;165:145–149. doi:10.1016/j.scriptamat.2019.02.035

[25] Senkov ON, Scott JM, Senkova SV, et al. Microstructure and room temperature properties of a high-entropy TaNbHfZrTi alloy. J Alloys Compd. 2011;509:6043–6048. doi:10.1016/j.jallcom.2011.02.171

[26] Senkov ON, Wilks GB, Scott JM, et al. Mechanical properties of Nb$_{25}$Mo$_{25}$Ta$_{25}$W$_{25}$ and V$_{20}$Nb$_{20}$Mo$_{20}$Ta$_{20}$W$_{20}$ refractory high entropy alloys. Intermetallics. 2011;19:698–706. doi:10.1016/j.intermet.2011.01.004

[27] Senkov ON, Scott JM, Senkova SV, et al. Microstructure and elevated temperature properties of a refractory TaNbHfZrTi alloy. J Mater Sci. 2012;47:4062–4074. doi:10.1007/s10853-012-6260-2

[28] Stepanov ND, Shaysultanov DG, Salishchev GA, et al. Structure and mechanical properties of a light-weight AlNbTiV high entropy alloy. Mater Lett. 2015;142:153–155. doi:10.1016/j.matlet.2014.11.162

[29] Guo NN, Wang L, Luo LS, et al. Microstructure and mechanical properties of refractory MoNbHfZrTi high-entropy alloy. Mater Des. 2015;81:87–94. doi:10.1016/j.matdes.2015.05.019

[30] Guo R, Zhang P, Pan J, et al. Achieving prominent high-temperature mechanical properties in a dual-phase high-entropy alloy: a synergy of deformation-induced twinning and martensite transformation. Acta Mater. 2024;264:119591. doi:10.1016/j.actamat.2023.119591

[31] Caillard D, Martin L. Thermally activated mechanisms in crystal plasticity. Oxford: Elsevier; 2003.

[32] Wang M, Lu Y, Wang T, et al. A novel bulk eutectic high-entropy alloy with outstanding as-cast specific yield strengths at elevated temperatures. Scr Mater. 2021;204:114132. doi:10.1016/j.scriptamat.2021.114132

[33] Flemings MC. Solidification processing. Metall Trans. 1974;5:2121–2134. doi:10.1007/BF02643923

[34] Luo Y, Zheng Q, Sun B, et al. Phase-selective transformation enabled coherent interfaces for coordinated deformation in FCC-laves eutectic high-entropy alloys. Mater Sci Eng A. 2026;953:149747. doi:10.1016/j.msea.2026.149747

[35] Ai C, Wang G, Liu L, et al. Effect of Ta addition on solidification characteristics of $CoCrFeNiTa_x$ eutectic high entropy alloys. Intermetallics. 2020;120:106769. doi:10.1016/j.intermet.2020.106769

[36] Chen T-W, Wu B-C, Kang Y-C, et al. The impact of grain boundary serration treatments on the creep deformation of Udimet-720Li superalloy. Mater Sci Eng A. 2025;924:147729. doi:10.1016/j.msea.2024.147729

[37] Zhang Z, Yuan L, Ma J, et al. Role of and < c+a > dislocations on the room-temperature grain boundary migration in a deformed Mg alloy. Int J Plast. 2024;172:103862. doi:10.1016/j.ijplas.2023.103862

[38] Li Z, Lv Q, Wei H, et al. Effects of RE (Nd, Ce, Y, La) on TiC(100)/Fe(110) interface based on first-principles calculations. Vacuum. 2022;205:111449. doi:10.1016/j.vacuum.2022.111449

[39] Tiller WA, Jackson KA, Rutter JW, et al. The redistribution of solute atoms during the solidification of metals. Acta Metall Mater. 1953;1:428–437. doi:10.1016/0001-6160(53)90126-6

[40] Lee J-L, Wang P-T, Lo K-C, et al. Effect of serrated grain boundary on tensile and creep properties of a precipitation strengthened high entropy alloy. Sci Technol Adv Mater. 2023;24:2158043. doi:10.1080/14686996.2022.2158043

[41] Campo KN, Wischi M, Rodrigues JFQ, et al. Directional solidification of the $Al_{0.8}CrFeNi_{2.2}$ eutectic high-entropy alloy. J Mater Res Technol. 2024;30:8874–8881. doi:10.1016/j.jmrt.2024.05.257

[42] Li H, Zhao Y, Song Z, et al. Serrated grain boundary modulation inhibits nano cracks propagation in pure magnesium: a phase field crystal and quasi in-situ EBSD study. Acta Mater. 2025;301:121573. doi:10.1016/j.actamat.2025.121573

[43] Chu F, Thoma DJ. Phase stability and defect structure of the C15 laves phase. Acta Mater. 1998;46:1759–1769. doi:10.1016/S1359-6454(97)00291-7

[44] Chai YW, Kato K, Yabu C, et al. Disconnections and Laves (C14) precipitation in high-Cr ferritic stainless steels. Acta Mater. 2020;198:230–241. doi:10.1016/j.actamat.2020.08.006

[45] Zhu JH, Liu CT. Defect structures in $ZrCo_2$ Laves phase. Acta Mater. 2000;48:2339–2347. doi:10.1016/S1359-6454(00)00014-8

[46] Misra A, Gibala R. Slip transfer and dislocation nucleation processes in multiphase ordered Ni-Fe-Al alloys. Metall Trans A. 1999;30:991–1001. doi:10.1007/s11661-999-0152-3

[47] Nilsen CF, Subramanian KN. Role of strain-rate and phase boundary geometry on the deformation behaviour of two-phase bicrystals of alpha-beta brass. J Mater Sci. 1984;19:768–776. doi:10.1007/BF00540447

[48] Markenscoff X. Driving forces on phase boundaries: 'The Eshelby principle for an interface'. Int J Fract. 2010;165:223–227. doi:10.1007/s10704-010-9526-1